

Tutorial: Deep learning prediction of thermophysical properties for liquid multicomponent alloys

Cite as: J. Appl. Phys. 134, 191101 (2023); doi: 10.1063/5.0173250

Submitted: 21 August 2023 · Accepted: 31 October 2023 ·

Published Online: 21 November 2023



View Online



Export Citation



CrossMark

R. L. Xiao, K. L. Liu, Y. Ruan, ^{a)} L. Hu, and B. Wei

AFFILIATIONS

MOE Key Laboratory of Materials Physics and Chemistry under Extraordinary Conditions, School of Physical Science and Technology, Northwestern Polytechnical University, Xi'an 710072, China

^{a)}Author to whom correspondence should be addressed: ruany@nwpu.edu.cn

ABSTRACT

The thermophysical properties of liquid metals and alloys are crucial to explore the intrinsic mechanisms of the solidification process, glass formation, and fluid dynamics. The deep learning approaches have emerged as powerful tools in numerous scientific fields and exhibit extraordinary accuracy in the estimation of physical properties and structural characteristics for various materials. In this Tutorial, focusing on the thermophysical properties of liquid multicomponent alloys, deep learning methods, including both supervised learning and active learning, are introduced. Combined with the verification from electrostatic and electromagnetic levitation experiments, the influences of training parameters and methods on the accuracy to obtain interatomic potential by deep learning are revealed on the basis of deep neural network algorithm. As a result, this prediction method of liquid state properties for multicomponent alloys exhibited the dual advantages of high accuracy derived from density functional theory and low computational cost associated with empirical potential.

Published under an exclusive license by AIP Publishing. <https://doi.org/10.1063/5.0173250>

I. INTRODUCTION

The investigation of thermophysical properties of liquid metals/alloys holds significant importance in various scientific and technological fields.^{1,2} Density is one of the most fundamental parameters of liquid metals/alloys and is crucial for applications, such as casting and metal forming processes. Specific heat capacity determines the amount of thermal energy required to raise the temperature of liquid metals/alloys, making it essential for designing efficient heat transfer and energy storage systems. Surface tension affects the wetting behavior and the capillary flow of liquid metals/alloys, influencing their ability to coat surfaces and form desired shapes. Viscosity affects the flow behavior and resistance to deformation of liquid alloys/metals, impacting their processability and performance in applications, such as lubrication and metal casting. Moreover, the study of thermophysical properties provides valuable insights into the fundamental understanding of liquid metals/alloys.³ Thus, understanding these properties is crucial for the development of advanced materials, optimization of industrial processes, and design of efficient heat transfer and energy storage systems.

Based on traditional contact measurement methods, researchers had made significant efforts to determine the thermophysical properties of metals and alloys.^{4–7} Those methods demonstrated a relatively accurate capacity to measure the thermophysical properties of metals or alloys with low melting points and stable chemical properties, whereas, while dealing with metals/alloys with high chemical activity, significant discrepancies are observed among different experiments, which can be attributed to contamination from a container wall or oxidation (as chemical reactions can occur even when the metals/alloys are in their solid state).⁸ Moreover, the traditional contact measurement methods are not suitable for accurately measuring the liquid thermophysical properties of metals/alloys with high melting points or under highly undercooled metastable states.

Benefiting from the development in containerless process technologies, such as electromagnetic levitation (EML)^{9–11} and electrostatic levitation (ESL),^{12–14} as well as simulation methods, such as molecular dynamics (MD)¹⁵ and density functional theory (DFT),¹⁶ there are increased opportunities for studying thermophysical and structural properties of liquid metals/alloys.

25 November 2023 09:19:03

Compared to the traditional contact measurement methods, the utilization of non-contact measurement in a levitation state significantly broadens the measurement range of the thermophysical properties. These approaches also provide advantages when dealing with metals/alloys that exhibit high chemical activity. Nonetheless, these methods alone cannot fully meet the enormous demand for establishing comprehensive thermophysical property databases for material genomes. For the simulation methods, they face the trade-off between accuracy and efficiency.¹⁷ The *ab initio* molecular dynamics (AIMD) based on DFT can accurately predict the dynamic behavior of metal/alloy systems without compositional restrictions. However, it is computationally expensive and only applicable to limited spatial and temporal scales. The classic MD based on empirical potentials is faster and can be applied to larger spatial and temporal scales. Nevertheless, its computational accuracy and transferability are deficient, and the development of empirical potentials is relatively hysteretic. The very few available empirical potentials for multicomponent alloys pose a hindrance to their scientific research and industrial development.

Advances in machine learning methods, such as deep neural network (DNN), have revolutionized the investigation of material properties, providing researchers with unprecedented accuracy.^{18–21} In this Tutorial, we will start by reviewing various measurement methods, encompassing both contact and non-contact techniques. We will then proceed to introduce the methodology of DNN, and the framework of a DeePMD-kit,¹⁷ and Deep Potential Generator (DP-GEN),²² powerful tools based on deep learning. Sections IV and V will specifically concentrate on the practical application of the DNN potential for an Ti–Ni–Cr–Al alloy, highlighting the impact of training details.

II. EXPERIMENTAL MEASUREMENT METHODS

A. Contact measurement methods

The contact measurement methods for determining the thermophysical properties of low-temperature liquid metals and alloys are relatively easy to implement. One widely used and reliable method for measuring the density is the Archimedes method. Figure 1(a) shows the schematic diagram of measurement. This method involves determining the density of the liquid metal/alloy by completely immersing a metal with a known density into the liquid metal/alloy being measured, following the principles of Archimedes. The density of the liquid metal/alloy ρ is obtained from

$$\rho = \frac{\rho_0}{1 + 3\alpha(T - T_0)} \frac{(m_0 - m_1)}{m_0}, \quad (1)$$

where ρ_0 is the density of the bulk metal at the corresponding temperature, m_0 is the mass of the bulk metal measured in the inert gas environment, m_1 is the mass of the bulk metal completely immersed in the liquid metal/alloy, α is the thermal expansion coefficient of the bulk metal, T is the experimental temperature, and T_0 is the room temperature.

Differential scanning calorimetry (DSC) is commonly used to determine the specific heat capacity of metals/alloys, employing the sapphire method. In the experiment, it is recommended to use a moderate heating rate (less than 10 K min^{-1}). By comparing the

heat flow of the metallic sample F_{sam} with that of the sapphire F_{spr} , the specific heat capacity at constant pressure of the metal/alloy C_p can be obtained using the following equation:

$$C_p = \frac{m_{\text{spr}} F_{\text{sam}}}{m_{\text{sam}} F_{\text{spr}}} C_{p,\text{spr}}, \quad (2)$$

where $C_{p,\text{spr}}$ is the specific heat capacity of the sapphire.

The sessile drop method is adopted to determine the surface tension σ of the liquid metals and alloys, as illustrated in Fig. 1(b). This method involves placing the liquid metals and alloys on a flat surface, and the surface tension is obtained by fitting the parameters of the Laplace equation. The coordinates of the drop liquid metals/alloys are expressed in the following form:

$$\frac{\rho g b^2 (h - z)}{\sigma} + \frac{1}{b} \frac{2\sigma - \rho g b^2}{\sigma} - \frac{\sin \theta}{x} = 0. \quad (3)$$

In the equation, g is the gravitational acceleration, h is the height of the drop, b is the radii of curvature at the drop apex, and θ is the contact angle. This method is applicable to liquid metals/

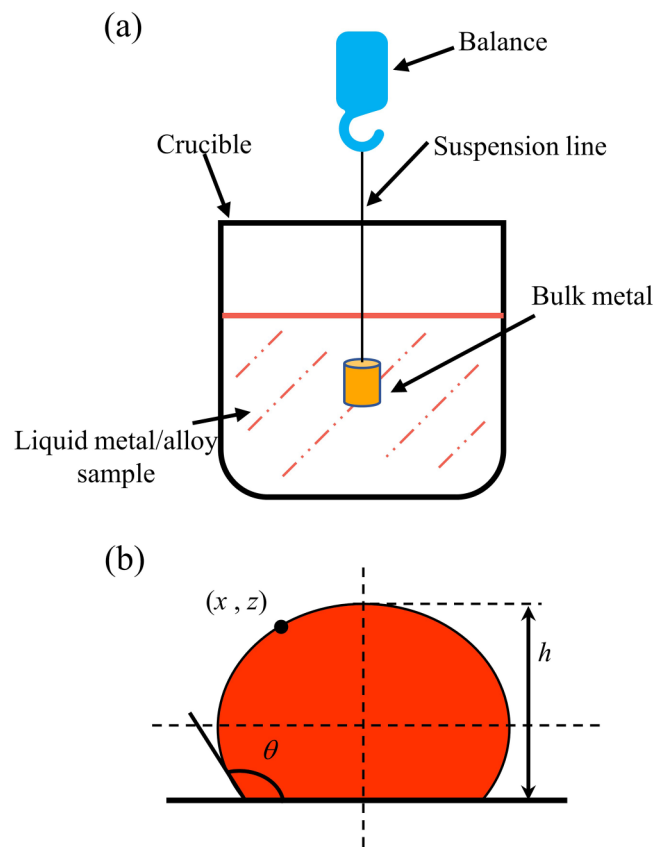


FIG. 1. Schematic illustration of the thermophysical property measurement through traditional methods: (a) density and (b) surface tension.

25 November 2023 09:19:03

alloys that do not wet with the substance ($\theta > 90^\circ$).²³ For the conditions where the liquid metals/alloys wet with the substance ($\theta < 90^\circ$), the pinned drop method²³ is recommended.

The viscosity of metallic melts can be determined using the damped torsional oscillation method.²⁴ During the measurement, the liquid sample is placed in a container suspended by a torsion suspension. By applying torque to the melt sample, its motion gradually dampens due to the absorption and dissipation of frictional energy in the liquid. Based on the amount of oscillation decay and time period, the viscosity η of the liquid sample can be calculated through the Schvidkovskii equation

$$\eta = \frac{\rho I^2 (\delta - \gamma \delta_0 / \gamma_0)^2}{\pi (mr)^2 \gamma} \left[1 - \frac{3\delta}{4\pi} - \frac{3\delta^2}{32\pi^2} - a + \left(b - \frac{c\delta}{2\pi} \right) \frac{2nr}{h} \right]^{-2}, \quad (4)$$

where I is the moment of inertia, δ and δ_0 are the damping logarithmic decrement of the container with the sample and the empty container, γ and γ_0 are the periods of oscillation of the container with the sample and the empty container, r is the radius of the container, a , b , and c are constants, h is the depth of the sample, and n is the number of horizon planes contacting with the liquid sample.

B. Non-contact measurement methods

In Sec. II A, we briefly introduced some of the traditional methods for obtaining thermophysical properties of liquid metals/alloys, whereas these traditional contact measurement techniques have limitations when dealing with materials that have high melting points or high chemical reactivity. For example, during the measurement process, the molten Ti tends to react with most crucibles, resulting in deviations in the measurement results. The measurements for the refractory metals/alloys, such as W and Re, are also an overwhelmingly difficult challenge. Additionally, the presence of container walls creates heterogeneous nucleation points for solidification, making it challenging to measure the properties of highly undercooled metastable metal/alloy melts. In this context, researchers have developed containerless processing techniques represented by electromagnetic and electrostatic levitation.

The electromagnetic levitation (EML) technique primarily utilizes high-frequency alternating current through a coil to create a potential well that stably levitates the sample, as shown in Fig. 2(a). The sample is melted and overheated by high-frequency induction heating. Cooling of the melted sample subsequently takes place through convective heat transfer with a helium gas. EML is only suitable for the measurement of the properties of electrically conducting samples. The density of the liquid droplets is determined by means of the optical dilatometry method,^{25,26} as illustrated in Fig. 2(b). In the process, a parallel laser beam is projected onto the sample from one side, while a high-speed CCD camera captures the projection image evolution of the sample on the plane perpendicular to the laser beam from the other side. The boundary curve, denoted as $r(\theta)$, of the sample projection image is fitted by Legendre polynomials,

$$r(\theta) = \sum_{i=0}^6 a_i P_i(\cos(\theta)). \quad (5)$$

Here, θ represents the azimuthal angle and a_i and P_i are the coefficient and Legendre polynomials of i order. Volume V of the liquid sample is calculated by integrating the boundary curve,

$$V = \frac{2}{3} q \pi \int_0^\pi r(\theta)^3 \sin(\theta) d\theta, \quad (6)$$

in which q is the scaling factor to transform the image volume to true volume. Finally, the density is achieved through

$$\rho = \frac{m}{V}. \quad (7)$$

Due to the oscillation of the metal/alloy melts under electromagnetic levitation conditions, the accuracy of density measurement can be affected. To mitigate this, multiple images are usually collected and averaged to minimize the impact of oscillation on measurement accuracy.

The drop calorimeter method²⁷ and the laser modulation calorimetry method²⁸ are usually used to measure the specific heat

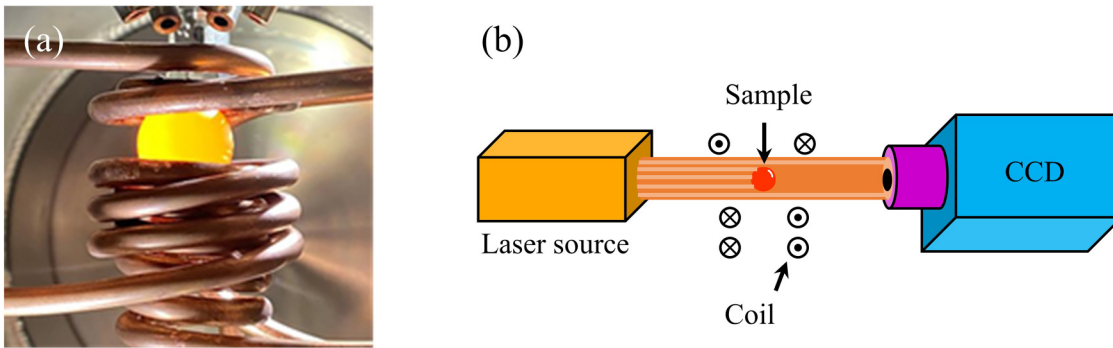


FIG. 2. Electromagnetic levitation: (a) a levitated stainless steel droplet and (b) a schematic illustration of the density measurement.

25 November 2023 09:19:03

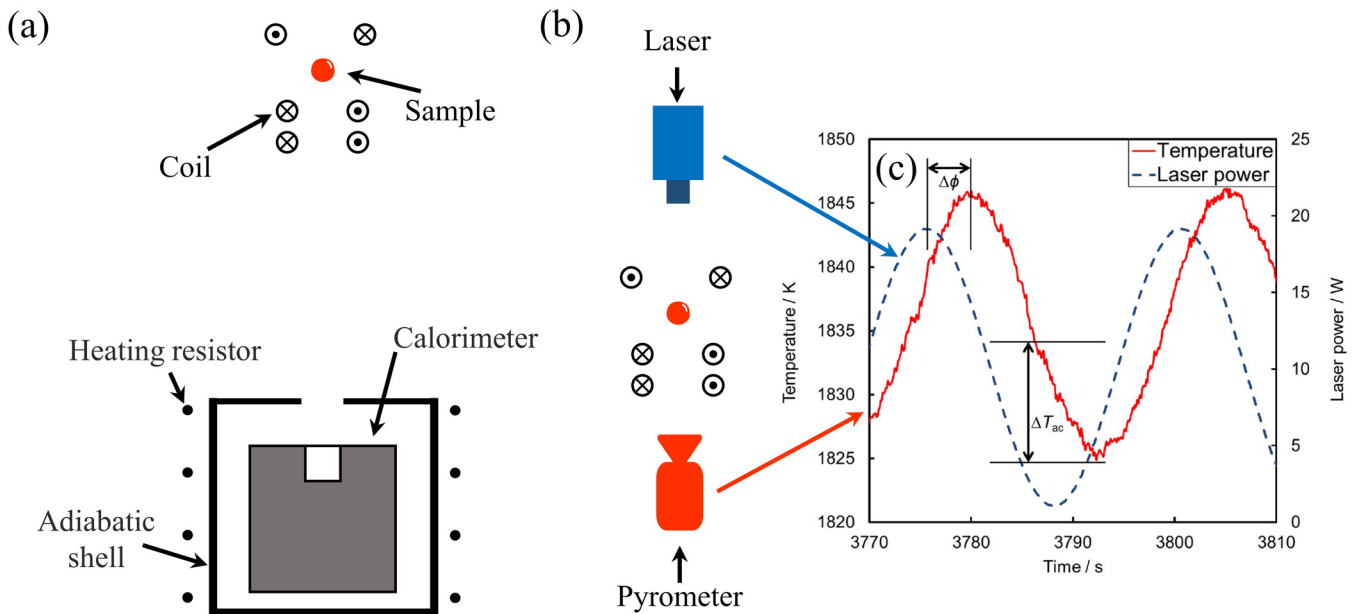


FIG. 3. Specific heat capacity measurement of the liquid sample with the EML facility: (a) drop calorimeter method, (b) laser modulation calorimetry method, and (c) laser power and sample temperature response.²⁸ (c) is reproduced with permission from Watanabe *et al.*, *J. Mol. Liq.* **324**, 115138 (2021). Copyright 2021 Elsevier.

25 November 2023 09:19:03

capacity (C_p) at constant pressure of liquid metals/alloys. The drop calorimeter method depends on an adiabatic calorimeter, and its illustration is shown in Fig. 3(a). Both of the calorimeter and the adiabatic shell are made of copper. When the sample reaches an ideal temperature, the current of the levitation coil is cut off and the sample will drop into the adiabatic calorimeter. The calorimeter and the shell are equipped with thermocouples to detect their temperatures. The central control computer automatically controls the heating resistor on the shell to achieve an adiabatic state of the system. The temperature of the calorimeter is monitored by two to four thermal resistors. Once the sample is dropped into the calorimeter, the heat released by the sample is absorbed by the calorimeter, causing the temperature of the calorimeter to rise from the initial temperature T_0 to the equilibrium temperature T_E . Hence, the law of energy conservation can be expressed as

$$H(T) - H(T_E) = \frac{M}{m} C_{P,Cu} (T_E - T_0) + \frac{Q_{lost}}{m}, \quad (8)$$

where $H(T)$ and $H(T_E)$ are the enthalpy of the sample at drop temperature and equilibrium temperature, respectively, M is the mass of the calorimeter, $C_{P,Cu}$ is the specific heat capacity of Cu, and Q_{lost} is the heat loss. The specific heat capacity can be derived by

$$C_p = \frac{\partial H}{\partial T} = \frac{\partial [H(T) - H(T_E)]}{\partial T}. \quad (9)$$

For the laser modulation calorimetry method,²⁸ as illustrated in Figs. 3(b) and 3(c), a modulation laser with a power of

$[P_0(1 + \cos\omega t)]$ is used to heat the sample from top. Simultaneously, the temperature of the sample is monitored by a pyrometer from the bottom. By measuring the phase shift $\Delta\phi$ between the laser power and temperature and temperature amplitude ΔT_{ac} , the specific heat capacity of the alloy can be derived through the following equation:

$$C_p = \frac{\alpha_T S_h A P_0}{\Delta T_{ac} \omega} f_c, \quad (10)$$

$$\Delta\phi = \arccos \left\{ \frac{\tau_c}{\omega} \left(\frac{1}{\tau_i \tau_e} - \omega^2 \right) f_c \right\}, \quad (11)$$

$$f_c = \left(1 + \frac{1}{\omega^2 \tau_e^2} + \omega^2 \tau_i^2 \right)^{-1/2}, \quad (12)$$

where α_T is the absorptivity, S_h is the area ratio of the laser irradiated part of the sample, A is the surface area of the sample, τ_e and τ_i are the external and internal thermal relaxation times, and f_c is the correction function. According to the Kirchhoff radiation law, the absorptivity is equal to emissivity ε_T . A static magnetic field is applied during the test to suppress convective flow.

Under the condition of EML, the liquid metal/alloy samples will be forced to oscillate under alternating electromagnetic fields. Based on this, the surface tension and the viscosity of the alloy can be measured by the oscillating drop method. The oscillation signal of the sample is acquired by a photodiode with a sampling frequency, usually ranging from hundreds of Hz to 20 000 Hz, which is much higher than the sample oscillation frequency. Figure 4(a)

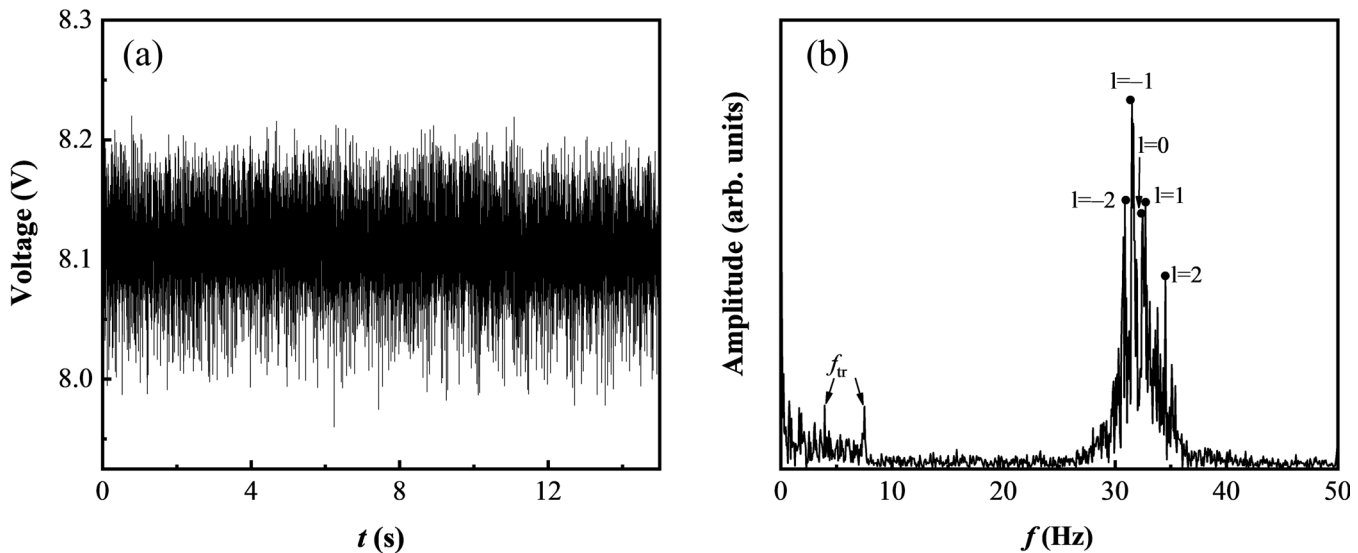


FIG. 4. Surface tension measurement of the liquid $\text{Ti}_{79}\text{Ni}_{10}\text{Cr}_6\text{Al}_5$ alloy with the EML facility: (a) oscillation signal and (b) the Rayleigh frequency.

illustrates a typical oscillation signal of a melted $\text{Ti}_{79}\text{Ni}_{10}\text{Cr}_6\text{Al}_5$ alloy close to its liquidus temperature with a sampling frequency of 10 000 Hz. The surface oscillation spectrum can be obtained by applying fast Fourier transformation (FFT) to the oscillation signal, as shown in Fig. 4(b). In the case where the sample is an ideal sphere and the droplet does not rotate, the surface tension of the sample oscillated with an angular frequency ω /line frequency f can be obtained through the Rayleigh equation^{23,29}

$$\sigma = \frac{3\omega^2 m}{32\pi} = \frac{3}{8}\pi m f^2, \quad (13)$$

whereas due to the non-ideal symmetry caused by factors, such as gravity and the levitation electromagnetic field generated by the coil during ground experiments, the sample deviates from the ideal spherical shape. To correct for the effects of gravity and the levitation electromagnetic field, Cummings and Blackburn³⁰ introduced a correction for the Rayleigh frequency,

$$f_R^2 = \frac{1}{5} \sum_{l=-2}^{l=2} f_{2,n}^2 - 2\bar{f}_{tr}^2, \quad (14)$$

in which l is the oscillation mode, $f_{2,n}$ is the frequency of the n th peak, and \bar{f}_{tr} is the mean translational frequency of droplet's center of mass. The viscosity of the sample can be estimated through the Egry model,³¹ which relates viscosity to the surface tension,

$$\eta = \frac{16}{15} \sqrt{\frac{M_A}{k_B T}} \sigma. \quad (15)$$

In this equation, M_A is the absolute atomic mass and k_B is the Boltzmann constant. For the EML experimental measurement of

viscosity, an electromagnetic field is applied to the sample to induce additional oscillations, and the damping time constant τ is determined. For an ideal sphere, the sample without an external force is related to the damping time constant,

$$\eta = \frac{\rho r^2}{5\tau} = \frac{3m}{20\pi r\tau}. \quad (16)$$

However, under terrestrial conditions, the damping effect and the internal convective flow result by a strong electromagnetic field prohibit the measurement of the viscosity. Therefore, a correction for the effect of the electromagnetic field on the viscosity is needed. It can be crudely corrected by introducing a magnetic viscosity η_{mag} term,²⁹

$$\eta = \frac{3m}{20\pi r\tau} + \eta_{mag} = \frac{3m}{20\pi r\tau} + \sigma_{ec} B^2 r^2, \quad (17)$$

where σ_{ec} denotes the electrical conductivity of the sample and B is the magnetic field. The viscosity obtained through Eq. (17) still significantly deviates from values determined through other experiments. This suggests that measuring the viscosity of liquid alloys via electromagnetic levitation in ground experiments is not feasible.

The electrostatic levitation (ESL) is a method of levitating a sample by using Coulomb force generated by an electrostatic field to counteract gravity on a charged object, as depicted in Fig. 5. Compared to electromagnetic levitation, electrostatic levitation has the following characteristics:

- (1) ESL enables the stable levitation of a wider range of materials, including oxides, semiconductors, and glasses, in addition to metallic materials.

25 November 2023 09:19:03

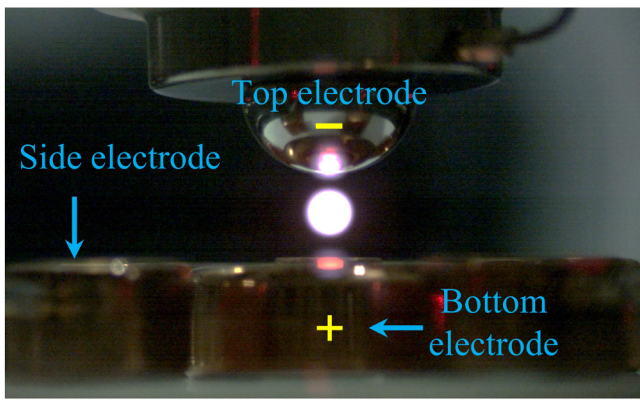


FIG. 5. Electrostatic levitation of a liquid Ti-Ni-Al alloy droplet.

- (2) Real-time detection of the sample position and the active control on the electrostatic field are deployed to achieve a stable levitation state of the sample because there is no potential well in an electrostatic field.
- (3) The electromagnetic stirring-induced forced convection inside the levitated droplet is eliminated in an electrostatic field.

Meanwhile, the droplet in a stable levitation state is close to a spherical shape due to surface tension, which is beneficial for the measurement of material thermophysical properties.

The density of the liquid sample can be determined using either the isothermal method or the continuous method. The principle for measuring the sample density under an electrostatic levitation state is similar to that of electromagnetic levitation. Since the energy of light radiation from the sample surface does not change significantly with temperature in the violet/ultraviolet region, we used a high-brightness light source equipped with a narrow-band filter as the background light to concentrate the background light in the violet band (400–450 nm). Figure 6 illustrates the density measurement process of Zr₂Ni melts by the isothermal method.³² Once the sample is melted, a real-time proportional-integral-differential (PID) feedback control system is activated to automatically adjust the power of the heating laser to maintain an isothermal temperature for the sample. Hundreds of images of the liquid sample are captured during the isothermal plateau by a high-speed black-white CCD camera. After that, the boundary of the sample is detected and fitted through Eq. (5). Then, the volume and density are obtained through Eqs. (6) and (7), respectively. In the continuous method, the sample photos are continuously captured during the cooling process after the sample is melted and the laser is turned off, in order to obtain the variation of the sample density with temperature.

Electrostatic levitation is performed under conditions of high vacuum. Therefore, the levitated sample undergoes only radiative cooling without experiencing contact or convective heat transfer. After the laser is turned off, during the cooling process, the sample

still satisfies the heat balance equation³³

$$\frac{C_p}{\varepsilon_T} = - \frac{AM\sigma_{SB}(T^4 - T_r^4)}{m R_c}, \quad (18)$$

where ε_T is the emissivity, M is the molar mass, σ_{SB} is the Stefan-Boltzmann constant, T_r is the environment temperature, and R_c is the cooling rate equal to $-dT/dt$, which can be obtained from the cooling curve by

$$t = a + bT^{-4}, \quad (19)$$

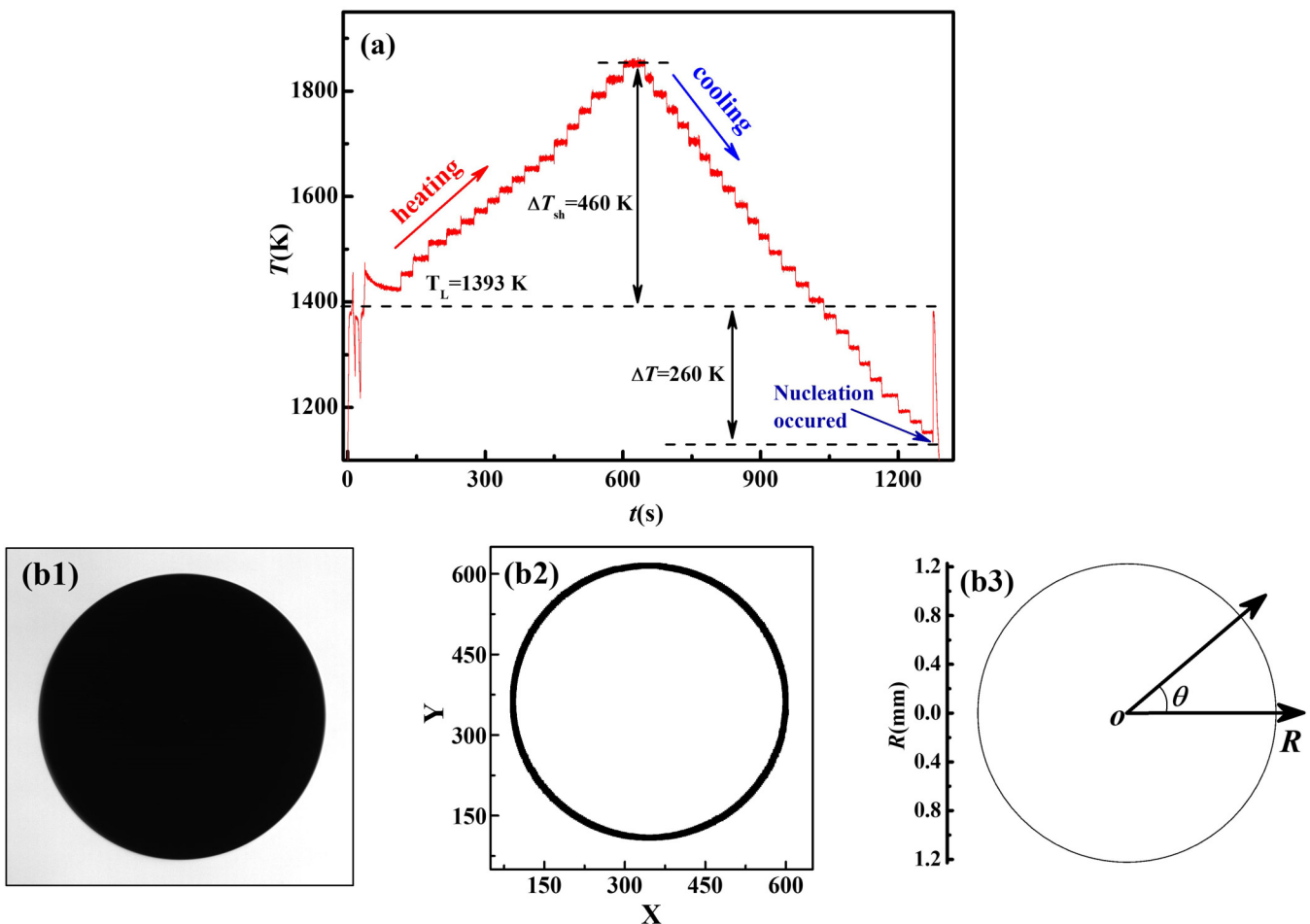
where a and b are constants. From Eqs. (18) and (19), the ratio of specific heat capacity and emissivity of the liquid sample can be obtained.

Under the electrostatic levitation conditions, when a sinusoidal excitation signal is superimposed on the levitation voltage signal and its frequency is close to the intrinsic oscillation frequency of the molten levitated sample, the resonance of the sample occurs, causing the melt to oscillate in a second-order axisymmetric mode. After removing the excitation signal, due to the effect of viscosity, the oscillation amplitude of the levitated melt will decay. Eventually, after a certain period of time, the oscillation will extinguish. The oscillation process of second-order axisymmetric and the oscillation signal are shown in Fig. 7.³² For second-order axisymmetric oscillation, the characteristic frequency can be obtained by performing a FFT on the oscillation signal. By substituting the characteristic frequency into Eq. (13), the surface tension of the liquid sample can be calculated. The damping time constant τ is acquired from the fitting of the decay curve after turning off the excitation through

$$r = a(\sin \omega t + \phi)\exp(-t/\tau) = a(\sin 2\pi ft + \phi)\exp(-t/\tau), \quad (20)$$

and the viscosity of the sample can be obtained by Eq. (16). For the surface tension, the influence of the electric field and gravity should be corrected.³⁴

From the above introduction, it is evident that gravity has a significant impact on the measurement of thermophysical properties in ground-based experiments. Therefore, researchers from various countries have developed measurement facilities on board parabolic aircrafts, sounding rockets, and space stations to realize micro-gravity environments. For example, the parabolic aircraft carried an EML facility developed by Deutsches Zentrum für Luft- und Raumfahrt (DLR),²⁹ while the sounding rocket carried an ESL furnace developed by the Japan Aerospace Exploration Agency (JAXA).¹² Building upon the technology accumulation from ground-based levitators, parabolic aircrafts, and sounding rockets, the National Aeronautics and Space Administration (NASA) collaborated with the European Space Agency (ESA), DLR, and JAXA to establish the EML and electrostatic levitation furnace (ELF) on-board International Space Station (ISS).^{35–40} As the China space station (CSS) enters into the full implementation stage, the ESL facility in a containerless material experiment rack on-board “Tianhe” core module has also applied to studies related to metal and non-metal material



25 November 2023 09:19:03

FIG. 6. Density of Zr_2Ni measured by an isothermal method: (a) T - t curve during measurement, (b1) the initial image captured by the black-white camera, (b2) the extracted boundary, and (b3) the fitted boundary by Legendre polynomials.³² Reproduced with permission from Wang *et al.*, Chem. Phys. Lett. **711**, 227–230 (2018). Copyright 2018 Elsevier.

processing, high undercooling research, and material thermo-physical properties.

III. DEEP LEARNING METHODOLOGY

A. Perceptron to a deep neural network

By referring to the neuron, the most fundamental structure of neuro, Rosenblatt⁴¹ proposed the concept of perceptron, which laid a good foundation of the neural network. The simplest model of a perceptron is expressed as Fig. 8. The relation between input value x and output y is

$$y = \varphi \left(\sum_i w_i x_i + b \right). \quad (21)$$

Here, φ is the activation function, w is the weight coefficient, and b is the offset value. Based on the perceptron model, by

adding multiple hidden layers, increasing the amount of output, and extending the activation function, the deep neural network (or a multi-layer perceptron) was built. In the deep neural network (DNN), the connection existed between every neuron in the upper layer and the lower layer. The entire DNN can be described as

$$\mathcal{F}(x) = W_0 \cdot \varphi_3(W_3 \cdot \varphi_2(W_2 \cdot \varphi_1(W_1 \cdot x + b_1) + b_2) + b_3) + b_0, \quad (22)$$

where W is the matrix of the weight coefficients. For any local neuron, it can still be expressed as a linear relationship by Eq. (21). By using appropriate activation functions, such as “tanh,” “gelu,” “relu,” “relu6,” “sigmoid,” “softplus,” etc., the expressive power and dimensionality reduction capabilities of the DNN are

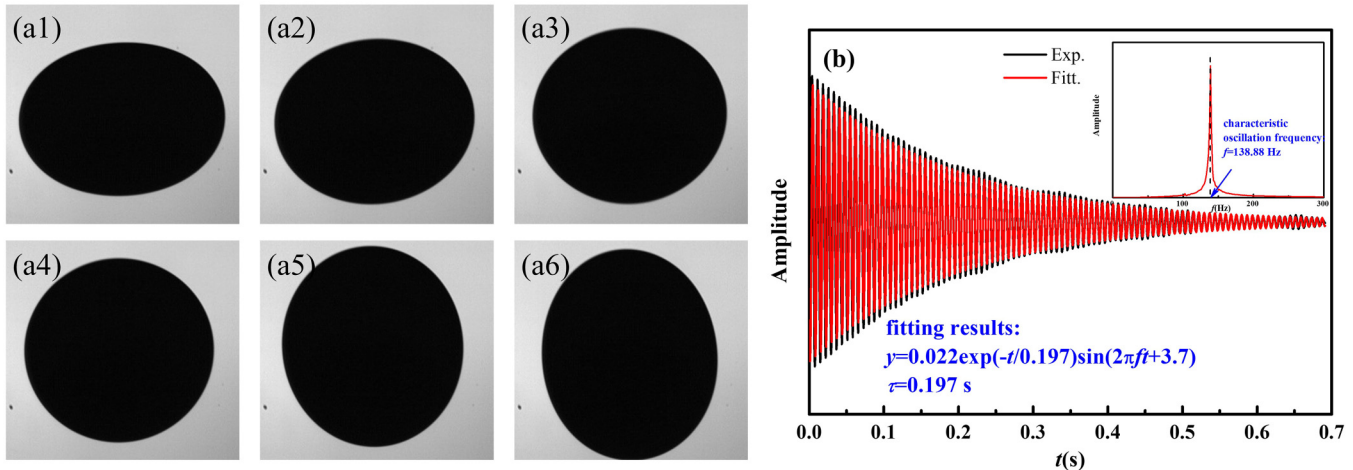


FIG. 7. Surface tension and viscosity of Zr₂Ni measured by an oscillating drop method: (a1)–(a6) oscillation process of second-order axisymmetric during excitation and (b) the detected decay curve after turning off the excitation, and the inserted figure is the characteristic oscillation frequency obtained by Fourier transformation.³² Reproduced with permission from Wang *et al.*, Chem. Phys. Lett. **711**, 227–230 (2018). Copyright 2018 Elsevier.

enhanced. The primary objective of the learning is to minimize the loss function L , which is given by

$$L = \mathcal{F}(x, W, b) - f(x). \quad (23)$$

We have to find the most appropriate W and b to fit the target function $f(x)$. The feed-forward propagation and the backward propagation were usually used to fit the expression of the DNN. The feed-forward propagation takes the output of the previous layer as the input for the next layer, calculating the output of each subsequent layer until reaching the output layer. The backward propagation, as the name suggests, involves calculating gradients in a feed-forward network by working backward from the last layer to the first. The gradient at each layer is calculated by combining the gradients of all subsequent layers using the chain rule of calculus.

B. Basic assumption

After a brief introduction to the deep learning methodology, here, we focus on the details of the DeePMD-kit, which is commonly used software for generating DNN potentials. As shown in Fig. 9, for atom i , its local environment in the cutoff radius r_c can be described by a descriptor¹⁷

$$D^i = \left\{ \frac{1}{r_{ij}}, \frac{x_{ij}}{r_{ij}}, \frac{y_{ij}}{r_{ij}}, \frac{z_{ij}}{r_{ij}} \right\}, \quad (24)$$

where (x_{ij}, y_{ij}, z_{ij}) are the relative Cartesian coordinates between atom i and j and $r_{ij} = |\mathbf{r}_{ij}| = |\mathbf{r}_i - \mathbf{r}_j|$. \mathbf{r}_{ij} is the localized coordinate containing the invariance of rotations and translations. The relation between \mathbf{r}_{ij} and the global relative coordinate \mathbf{r}_{ij}^0 can be

expressed as⁴²

$$\mathbf{r}_{ij} = \mathbf{r}_{ij}^0 \cdot R_i. \quad (25)$$

In the equation above, R_i is the rotation matrix, defined as

$$R_i = \{\mathbf{M}_{i1}, \mathbf{M}_{i2}, \mathbf{M}_{i3}\}, \quad (26)$$

$$\mathbf{M}_{i1} = \mathbf{M}(\mathbf{r}_{i,a(i)}), \quad (27)$$

$$\mathbf{M}_{i2} = \mathbf{M}(\mathbf{r}_{i,b(i)} - (\mathbf{r}_{i,b(i)} \cdot \mathbf{M}_{i1})\mathbf{M}_{i1}), \quad (28)$$

$$\mathbf{M}_{i3} = \mathbf{M}_{i1} \times \mathbf{M}_{i2}, \quad (29)$$

in which \mathbf{M} represents the normalizing operation to a vector, i.e., $\mathbf{M}(\mathbf{r}_{ij}) = \mathbf{r}_{ij}/r_{ij}$. $a(i)$ and $b(i)$ are the subsets of the nearest neighbor list, which is inside the r_c .

The energy of the system consisting of N atoms can be counted from the energy of every single atom. After parameterizing the system's configuration space, the total energy of the system is given as

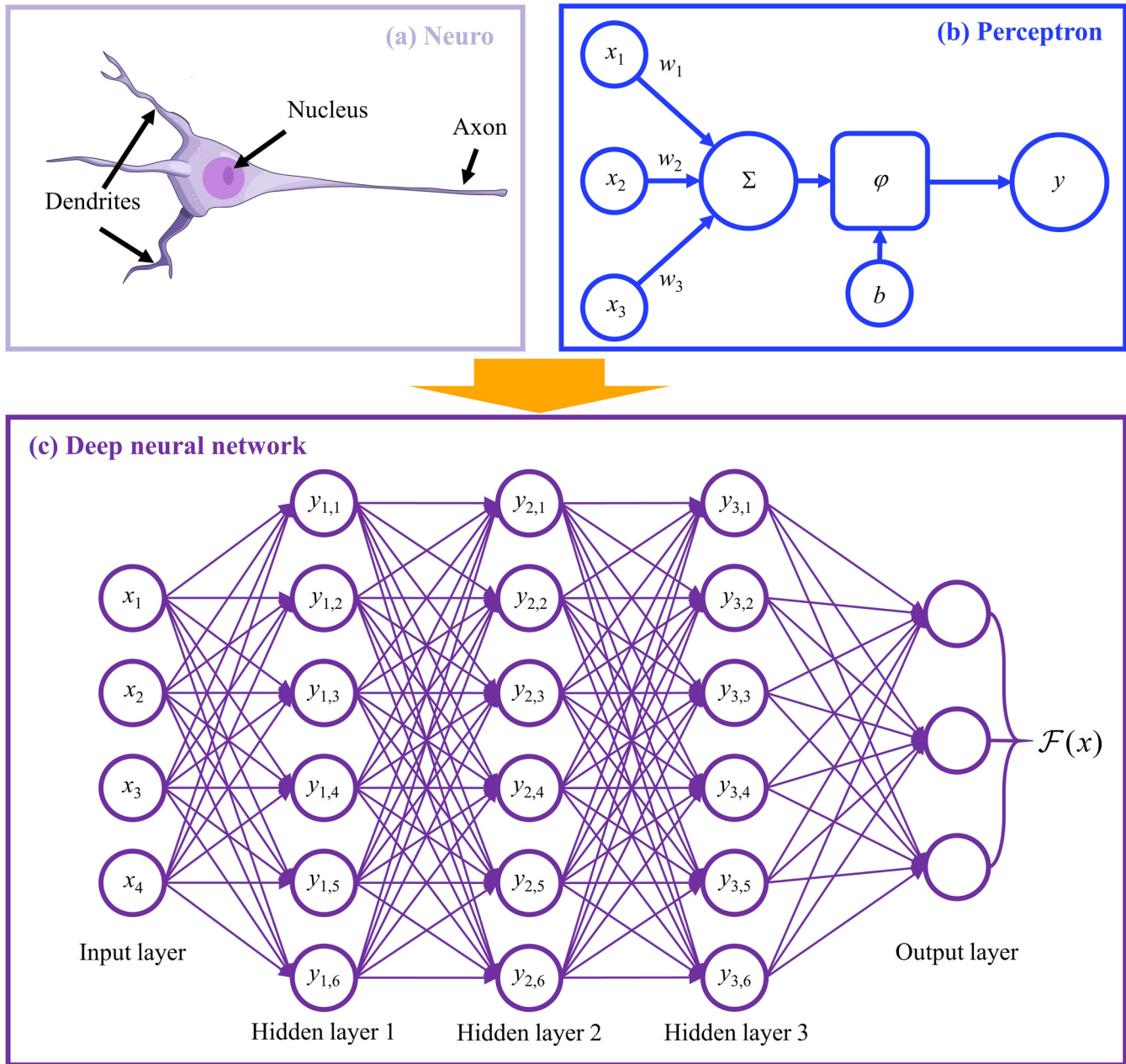
$$E = \sum_i E_i = \sum_i \mathcal{N}(D^i), \quad (30)$$

where \mathcal{N} is the multilayer perceptron with a hidden layer. Force \mathbf{F}_i on the atom i can be derived from the energy,

$$\mathbf{F}_{i,\chi} = -\frac{\partial E}{\partial r_{i,\chi}}, \quad (31)$$

where χ represents the component on the x , y , or z direction. If periodic boundary conditions are applied on the system, the virial

25 November 2023 09:19:03



25 November 2023 09:19:03

FIG. 8. Structures of (a) neuron, (b) perceptron, and (c) deep neural network.

tensor Ξ of the system can also be derived as

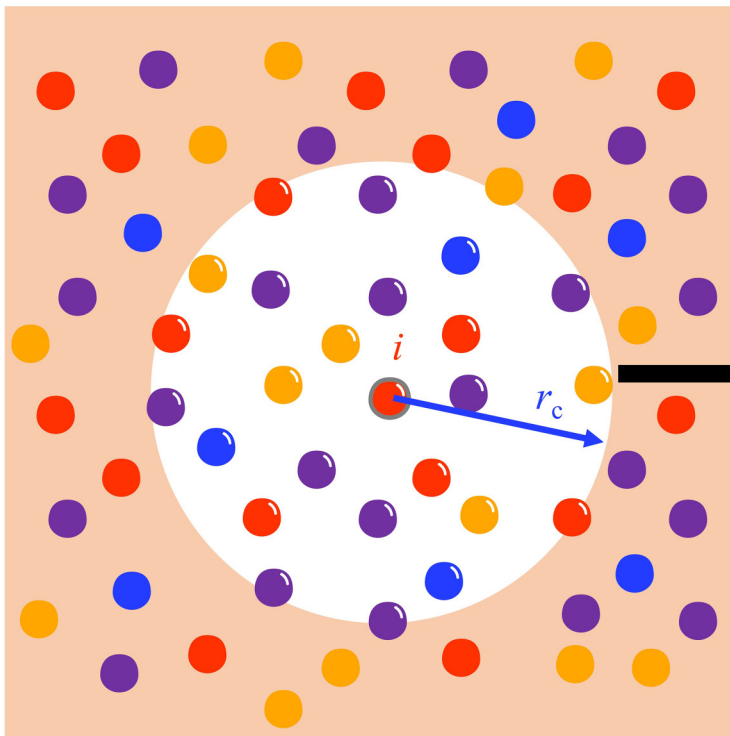
$$\Xi_{\alpha\beta} = - \sum_{\gamma} \frac{\partial E}{\partial h_{\gamma\alpha}} h_{\gamma\beta}, \quad (32)$$

where β and γ also represent the components of different directions and h denotes the basis vector. Loss function L is defined as the

sum of mean square errors of the predicted energy, force, and virial tensor,

$$L = \frac{p_E}{N} \Delta E^2 + \frac{p_F}{3N} \sum_i |\Delta F_i|^2 + \frac{p_\Xi}{9N} \|\Delta \Xi\|^2, \quad (33)$$

where ΔE , ΔF_i , and $\Delta \Xi$ are root mean square (RMS) errors and p_E ,



Local environment descriptor:

$$D^i = \left\{ \frac{1}{r_{ij}}, \frac{x_{ij}}{r_{ij}}, \frac{y_{ij}}{r_{ij}}, \frac{z_{ij}}{r_{ij}} \right\}$$

Total energy of system:

$$E = \sum_i E_i = \sum_i \mathcal{N}(D^i)$$



FIG. 9. Description for local environment and system energy.

p_f and p_ξ are prefactors of energy, force, and virial, respectively. The DNN will automatically find the $\{W, b\}$ in the training process that minimizes the loss function; i.e.,

$$\min_{\{W,b\}} L(p_e, p_f, p_\xi). \quad (34)$$

C. Training a DNN potential

For the DeepModeling series, DeepMD-kit¹⁷ and DP-GEN²² are commonly used to obtain the DNN potential. The DeePMD-kit is open-source software that is interfaced with TensorFlow. It primarily utilizes supervised learning methods to automatically derive the potential energy surface. Figure 10 provides a schematic illustration of the training procedure. The first step of the training entails preparing the training datasets, which can be generated from both DFT calculation (e.g., VASP, Gaussian, ABACUS, Quantum-Espresso, and CP2K) and MD calculation (e.g., LAMMPS). The correspondence output files needed to be transformed into a required format, incorporating information, such as box, atomic type, atomic coordination, energy, force, and virial. The data format conversion can easily be implemented through dpdata software.⁴³

After the training datasets were prepared, the training was carried out by means of the DeePMD-kit. The loss function was evaluated through feed-forward propagation during the

computation of the system energy, the atomic force, and the virial, and the derivatives of the loss function with respect to the parameters $\{W, b\}$ were also automatically computed by TensorFlow through backward propagation. The training process was managed by the predetermined control parameters specified in a JSON file. By taking the training process for H₂O DNN potential as a reference, an example of this file is provided. The complete script can be found in the website.⁴⁴ The first section is to give a general statement of the training system. It includes the atomic types and masses, which must match the order used in the initial DFT or MD calculations. For example,

```
"type_map": ["O", "H"],  
"mass_map": [15.9994, 1.00794].
```

Next, the descriptor section defines how the embedding net converts the atomic coordinate information into a descriptor with translation and rotation symmetries. In the given example,

```
"descriptor": {  
    "type": "se_e2_a,"  
    "sel": [46, 92],  
    "rcut_smth": 0.5,  
    "rcut": 6.0,  
    "neuron": [25, 50, 100].  
}
```

In the above definition, the type of descriptor is "se_e2_a," the two-body embedding descriptor of the Deep Potential Smooth

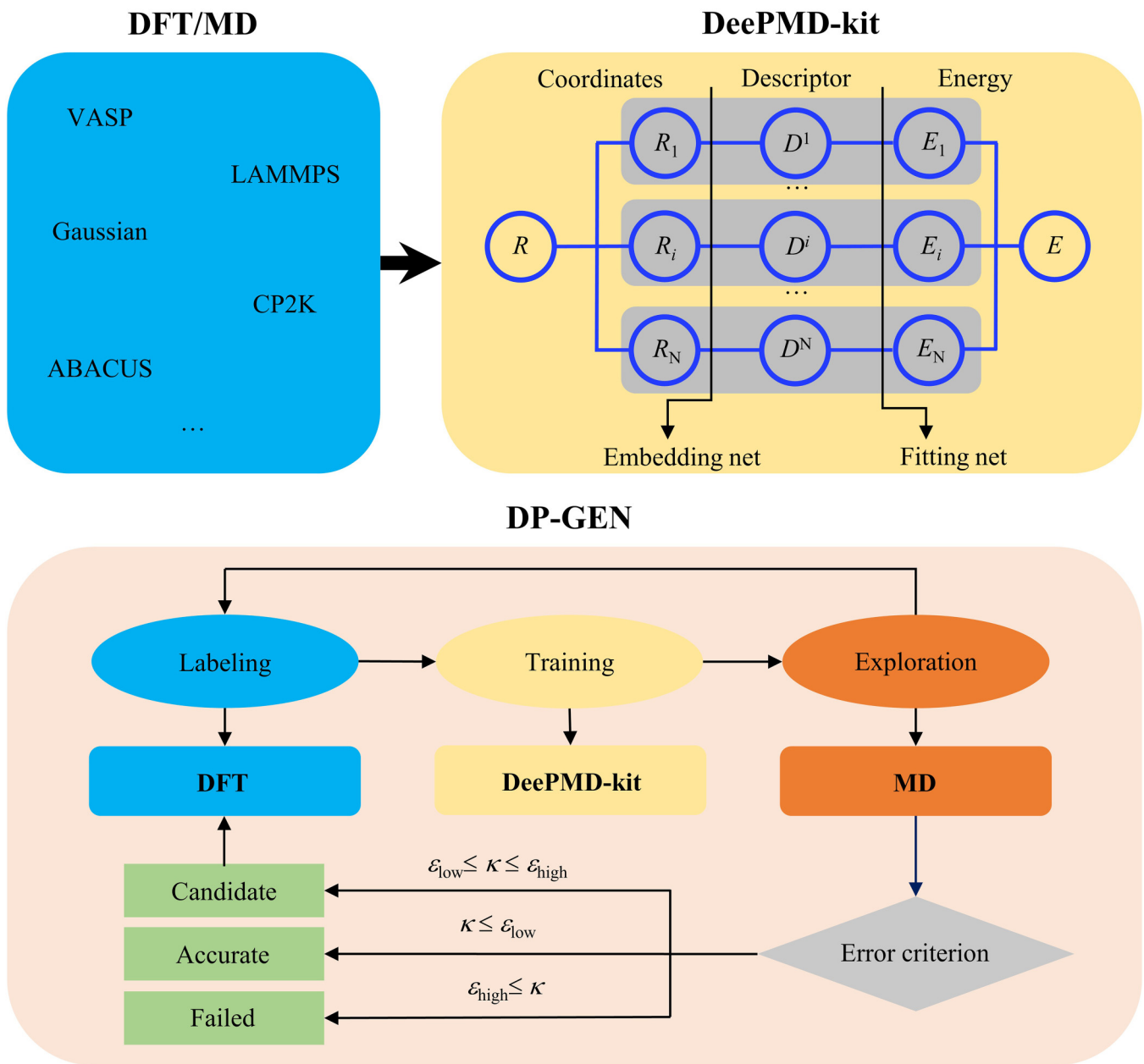


FIG. 10. Schematic illustration of the training procedure in DeePMD-kit and DP-GEN.

Edition (DeepPot-SE). In addition, the descriptors, such as “se_e2_r,” “se_e3,” “se_atten,” and “hybrid,” etc., can also be chosen and defined. Their difference was introduced in Ref. 42. The “sel” indicates the expected maximum number of O and H neighbor atoms of an atom in the cutoff radius r_c . The “rcut_smth” defines where to start the smoothing. In this script, an “embedding net” with 25, 50, and 100 neurons in each of the three hidden

layers was used. After setting the descriptor, the “fitting_net” is defined to fit the system energy. In the given example,

```
“fitting_net”:
  “neuron”: [240, 240, 240].
```

The “fitting_net” with 240, 240, and 240 neurons in each of the three hidden layers was used to fit the system

energy. The subsequent section sets the learning parameters. In this example,

```

"learning_rate": {
  "type": "exp",
  "start_lr": 0.001,
  "decay_steps": 5000,
  "stop_lr": 3.51e-08
},
"loss": {
  "type": "ener",
  "start_pref_e": 0.02,
  "limit_pref_e": 1,
  "start_pref_f": 1000,
  "limit_pref_f": 1,
  "start_pref_v": 0,
  "limit_pref_v": 0
},
"numb_steps": 1 000 000.

```

In this case, the learning parameters are set 1×10^6 epochs with an exponentially decaying learning rate from 1.00×10^{-3} to 3.51×10^{-8} are set. The learning rate decays every 5000 steps. Generally, the “numb_steps” $\geq 200 \times \text{decay_steps}$ is suggested. In the section “loss,” the prefactors of energy p_e , force p_f , and virial p_v in Eq. (33) were defined. Although the prefactors of “virial” in the example are 0, we emphasize that appropriate values should be set for the DNN potential train for the computation of liquid thermophysical properties. The significance of the “virial” will be tested in the following context.

The DP-GEN is an open-source concurrent learning platform and software package for the generation of DNN potentials in a way that minimizes the computational cost and human intervention.²² The usage of the DP-GEN required two JSON files: machine.json to specify the machine environment⁴⁵ and param.json to set the training procedure.⁴⁶ Its procedure is also illustrated in Fig. 10. Several successive iterations are involving in the process of the generation of DNN potentials. Each iteration is composed of three parts: training, exploration, and labeling. Similar to the DeePMD-kit, datasets containing some preparatory configurations are required, generated from DFT calculation. Initially, the DP-GEN trains several initial DNN potential models based on the knowledge from the initial configurations by invoking a DeePMD-kit (its control parameters consist of the above). Then, utilizing these trained DNN potential models, the DP-GEN conducts free exploration under the specified conditions through molecular dynamics simulations. The MD can be controlled by the following commands:

```

{
  "temps": [100],
  "press": [1.0],
  "trj_freq": 10,
  "nsteps": 300,
  "ensemble": "npt."
}

```

This example indicates that the system will run for 300 epochs under a condition of temperature 100 K and pressure 1 bar (unit metal) with the isothermal-isobaric (NPT) ensemble. The

multiple temperatures and pressures are available through commands, such as

```

{
  "temps": [100, 200, 300],
  "press": [1.0, 10.0, 100.0]
}

```

The DP-GEN will ransack all constitutions involving (100 K, 1 bar), (100 K, 10 bars), (100 K, 100 bars), (200 K, 1 bar), etc. The ensemble can also change to a canonical (NVT) ensemble. In addition to the MD, the MD with enhanced sampling techniques, the Markov chain Monte Carlo (MCMC) approach, and the genetic algorithm (GA) are also available during the exploration stage.²² The sampler will sample the MD trajectories every “trj_freq” step. At the labeling stage, the DP-GEN compares the differences in atomic forces predicted by different DNN potential models. Here, we define κ representing the maximal standard deviation of the atomic force. The κ values below the lower boundary ε_{low} are classified as accurate, those above the upper boundary $\varepsilon_{\text{high}}$ are classified as fail, and those between the lower boundary and the upper boundary $\varepsilon_{\text{low}} \leq \kappa \leq \varepsilon_{\text{high}}$ are identified as a candidate. The upper and lower bound of the trust levels can be set by

```

"model_devi_f_trust_lo": 0.05,
"model_devi_f_trust_hi": 0.15.

```

The lower boundary ε_{low} should not be arbitrarily small to avoid conducting DFT calculations on structures that have already been accurately predicted, as it would provide no new knowledge for the model and waste computational resources. The upper boundary $\varepsilon_{\text{high}}$ should not be arbitrarily big either. The unphysical configurations caused by the extreme differences are often difficult to converge in self-consistent field iterations in the DFT calculations. The candidate configurations will be regarded as the new initial configurations of the DFT simulation and pass them into the DFT simulations. After that, the new configurations by the DFT simulations will act as the new initial configurations added into the training datasets and start a new training—exploration—labeling cycle until the set maximum number of cycles is reached. Theoretically, under appropriate strategies, the predictive accuracy of multiple DNN potential models generated by DP-GEN should be very close. Any of them could be used for further MD simulations.

After generating the DNN potential model using DeePMD-kit/DP-GEN, it is crucial to validate the potential to prevent overfitting. As shown in Fig. 11, although the overfitting models can accurately replicate the data in the training dataset, they show significant errors when they predict the configurations in the validation dataset. For the well-trained model, the error in predicting the validation dataset should be roughly the same with the error in predicting the training set (the same order of magnitude). The validation dataset should be different from the training dataset; i.e., the AIMD simulation of a liquid alloy under 1500 and 2500 K is used for the training dataset, and the AIMD relaxation process of a different structure under 2000 K is suggested to be used for the validation dataset. To further illustrate the deep learning methods, we will use liquid Ti₇₉Ni₁₀Cr₆Al₅ multicomponent alloys as examples in Secs. IV and V to demonstrate the training of DNN potential and the acquisition of liquid properties through the above introduced deep learning tools.

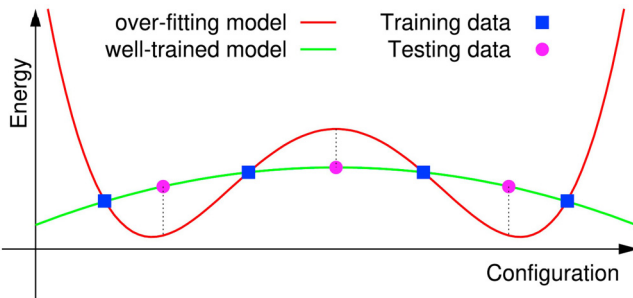


FIG. 11. Schematic illustration of over-fitting.¹⁷ Reproduced with permission from Wang *et al.*, Comput. Phys. Commun. **228**, 178–184 (2018). Copyright 2018 Elsevier.

IV. TRAINING FOR DNN POTENTIAL

The key to predicting the liquid thermophysical properties of multicomponent alloys via the deep learning method lies in developing a DNN potential. Before training, it is crucial to prepare training datasets with a sufficient number of configurations. The layering/clustering behavior of atoms, as shown in Fig. 12, is usually observed in simulations that use DNN potentials trained from datasets with either too few configurations or too many similar configurations. This problem can be solved by adding configurations that are significantly different from those in the original training dataset. In order to clarify the impact of different training parameters and tools on the prediction of liquid properties of materials, we trained multiple DNN potentials for the liquid $Ti_{79}Ni_{10}Cr_6Al_5$ multicomponent alloys. The differences between

the DNN potentials have been listed in Table I. In the training, the numbers of the embedding and fitting net were (25, 50, 100) and (240, 240, 240), respectively. Exponentially decaying learning rates from 1.00×10^{-3} to 3.51×10^{-8} were trained in a NVIDIA TESLA V100 TENSOR CORE GPU. For the liquid $Ti_{79}Ni_{10}Cr_6Al_5$ alloy, we trained four DNN potentials involving DPT1-1, DPT1-2, DPT1-3, and DPT1-4 to demonstrate the influence of “rcut_smth,” “virial,” and the training methods on the accuracy of predicting liquid alloy thermophysical properties of the DNN potentials. DPT1-1, DPT1-2, and DPT1-3 were all trained based on the same training set and validation set. The training datasets mainly contain 9×10^4 configurations of a liquid $Ti_{79}Ni_{10}Cr_6Al_5$ alloy system (200 atoms) at 2500, 2100, 1700, 1400, and 1200 K, respectively. Moreover, 5000 steps of simulation for $Ti_{70}Ni_{10}Cr_{10}Al_{10}$ and $Ti_{40}Ni_{20}Cr_{20}Al_{20}$ alloy melt systems (200 atoms) at 2500, 1850, and 1200 K were added to the training data to improve the accuracy of DNN potential. The validation datasets contain 1×10^4 configurations of a liquid $Ti_{79}Ni_{10}Cr_6Al_5$ alloy system, which were not included in the training datasets. Both training datasets and validation datasets were generated by AIMD in VASP. The Projector-Augmented-Wave (PAW) pseudo-potentials and the Perdew–Burke–Ernzerhof (PBE) gradient approximation to the exchange-correlation functional were adopted to describe the atom interaction. Only the Γ point was used to sample the Brillouin zone, and the energy cutoff of 300 eV was set. The time step was 3 fs. The AIMD simulations were performed using the periodic boundary conditions and the canonical (NVT) ensemble with the Nosé–Hoover thermostat.

In the training of DPT1-4, the initial training datasets consisted of 1×10^4 configurations of the liquid $Ti_{79}Ni_{10}Cr_6Al_5$ alloy system (200 atoms) at 2500 K. At the exploration stage, the LAMMPS was employed. The configurations generated by MD were classified according to the model deviations’ lower boundary

25 November 2023 09:19:03

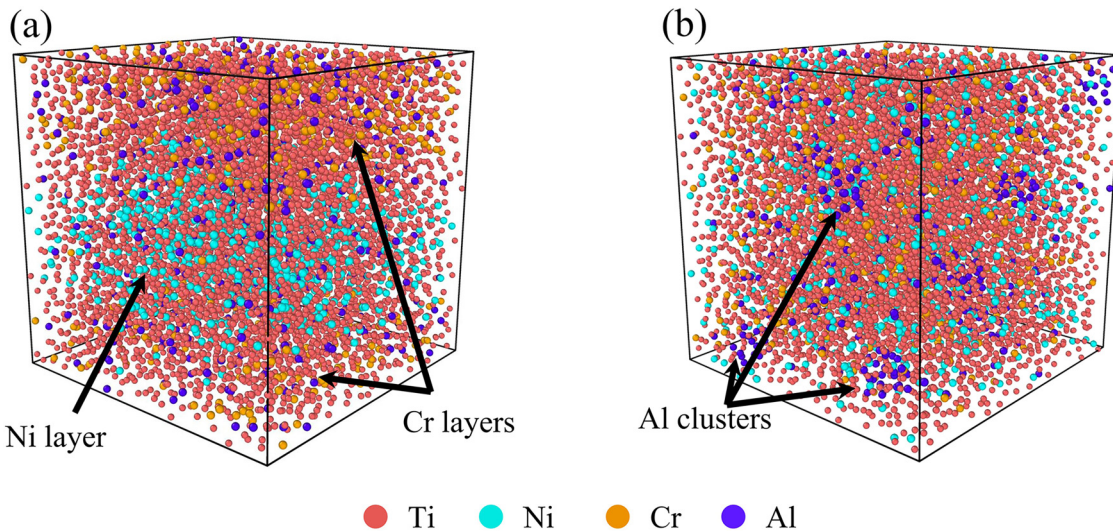


FIG. 12. Snapshots of the liquid $Ti_{79}Ni_{10}Cr_6Al_5$ alloy with 8100 atoms generated by simulations using DNN potentials that are trained from datasets without enough configurations: (a) layering behavior and (b) clustering behavior.

TABLE I. Training details of DNN potentials.

Model	System	Software	rcut_smth (Å)	rcut (Å)	Virial	Configuration
DPT1-1	$\text{Ti}_{79}\text{Ni}_{10}\text{Cr}_6\text{Al}_5$	DeePMD-kit	0.5	6	Yes	$\text{Ti}_{79}\text{Ni}_{10}\text{Cr}_6\text{Al}_5: 9 \times 10^4$
DPT1-2	$\text{Ti}_{79}\text{Ni}_{10}\text{Cr}_6\text{Al}_5$	DeePMD-kit	5.8	6	No	$\text{Ti}_{70}\text{Ni}_{10}\text{Cr}_{10}\text{Al}_{10}: 1.5 \times 10^4$
DPT1-3	$\text{Ti}_{79}\text{Ni}_{10}\text{Cr}_6\text{Al}_5$	DeePMD-kit	5.8	6	Yes	$\text{Ti}_{40}\text{Ni}_{20}\text{Cr}_{20}\text{Al}_{20}: 1.5 \times 10^4$
DPT1-4	$\text{Ti}_{79}\text{Ni}_{10}\text{Cr}_6\text{Al}_5$	DP-GEN	5.8	6	Yes	Initial: 1×10^4 $\text{Ti}_{79}\text{Ni}_{10}\text{Cr}_6\text{Al}_5$ Active learning: 6.99×10^3 $\text{Ti}_{79}\text{Ni}_{10}\text{Cr}_6\text{Al}_5$ $\text{Ti}_{70}\text{Ni}_{10}\text{Cr}_{10}\text{Al}_{10}$ $\text{Ti}_{40}\text{Ni}_{20}\text{Cr}_{20}\text{Al}_{20}$

and upper boundary [$\varepsilon_{\text{low}}, \varepsilon_{\text{high}}$], which were set as [0.15, 0.30] eV Å⁻¹. At the labeling stage, the DP-GEN software will automatically and randomly choose at most 1000 configurations, which are classified as candidates, and the VASP was employed to carry out the DFT calculations. K-points in the Brillouin zone are sampled by the Monkhorst–Pack Mesh with a grid spacing of 0.5 Å⁻¹. The DPGEN ran for ten iterations, during which the liquid $\text{Ti}_{79}\text{Ni}_{10}\text{Cr}_6\text{Al}_5$ alloy was explored at different temperatures from iteration 0 to 2 and 5 to 9, and liquid $\text{Ti}_{70}\text{Ni}_{10}\text{Cr}_{10}\text{Al}_{10}$ and

$\text{Ti}_{40}\text{Ni}_{20}\text{Cr}_{20}\text{Al}_{20}$ alloys were explored in iterations 3 and 4, respectively.

After generating the DNN potentials, their quality was assessed using validation datasets consisting of 2000 configurations of a liquid $\text{Ti}_{79}\text{Ni}_{10}\text{Cr}_6\text{Al}_5$ alloy at 2500, 2100, 1700, 1400, and 1200 K, which were not included in the training datasets. The system energy and the atomic force of those configurations are shown in Fig. 13. The root mean square (RMS) error of the predicted energy and force compared with the AIMD results is in

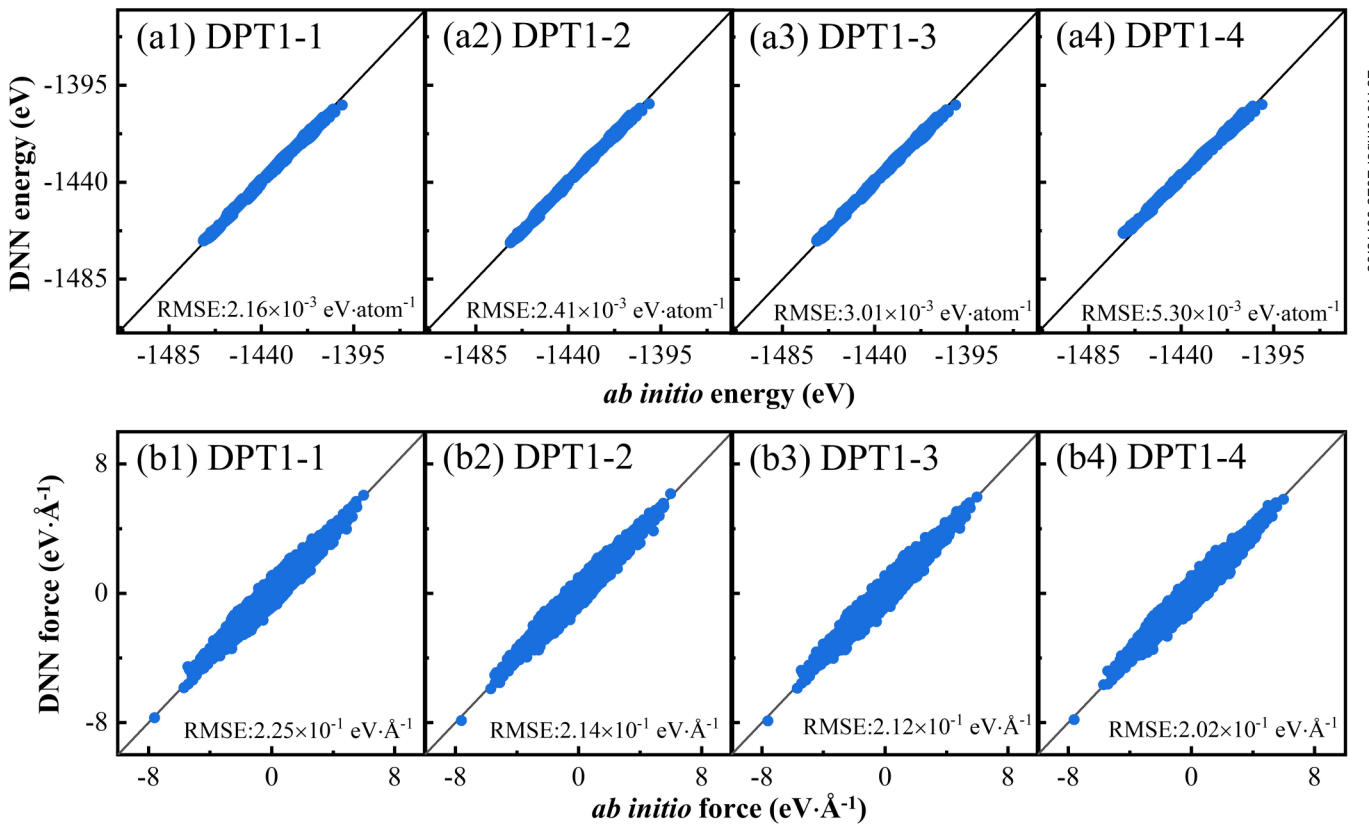


FIG. 13. Correlations between AIMD and DNN data: (a1)–(a4) energy and (b1)–(b4) force.

25 November 2023 09:19:03

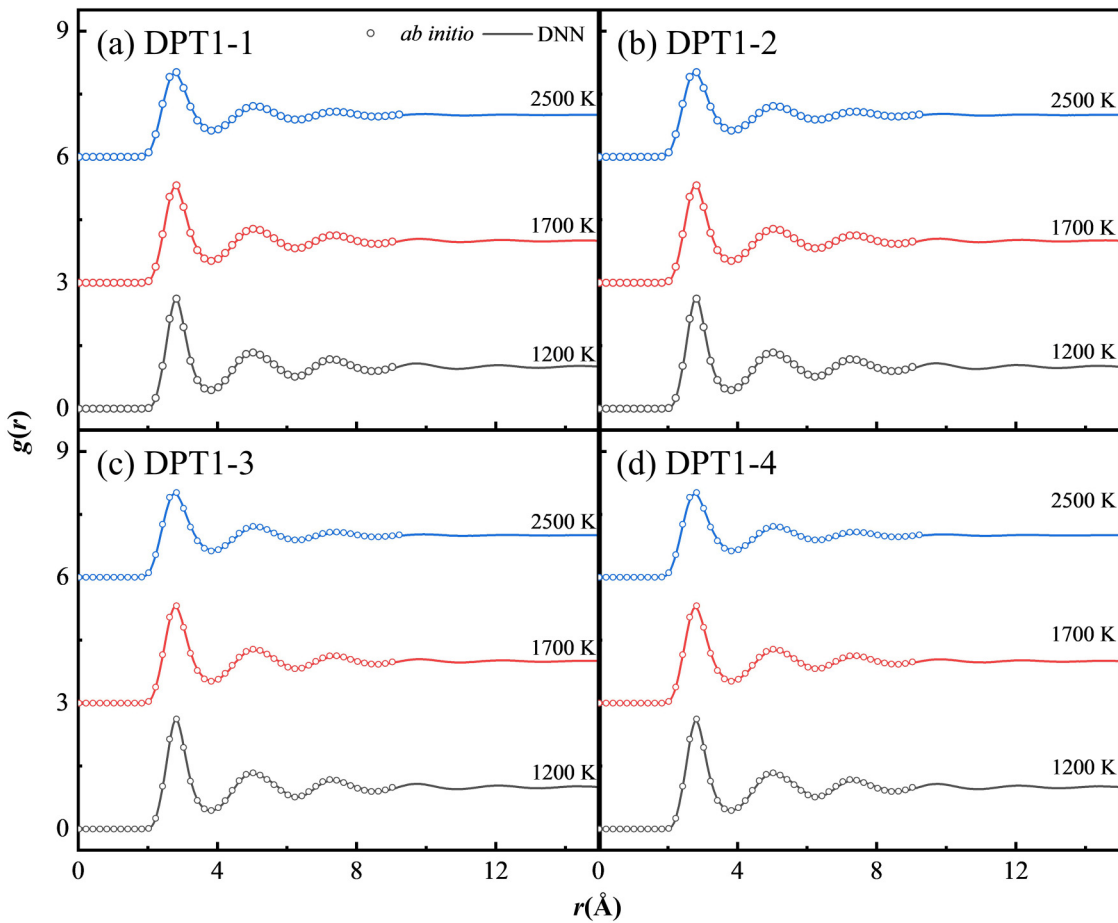


FIG. 14. Liquid structural characteristics of the $\text{Ti}_{79}\text{Ni}_{10}\text{Cr}_6\text{Al}_5$ alloy calculated by different DNN potentials: (a) DPT1-1, (b) DPT1-2, (c) DPT1-3, and (d) DPT1-4.

25 November 2023 09:19:03

10^{-3} eV atom $^{-1}$ and 10^{-1} eV Å $^{-1}$ order. Furthermore, as shown in Fig. 14, the predicted pair distribution functions (PDFs) of the liquid alloy by DNN potentials were also in accord with the AIMD results. This demonstrates that the DNN potentials achieve sufficient accuracy in the prediction of the energy, atomic force, and liquid structure of the liquid $\text{Ti}_{79}\text{Ni}_{10}\text{Cr}_6\text{Al}_5$ alloy.

V. CALCULATION OF LIQUID THERMOPHYSICAL PROPERTIES

After the DNN potentials were generated, LAMMPS was used to conduct MD simulations with the trained DNN potentials in order to acquire the thermophysical properties of the liquid $\text{Ti}_{79}\text{Ni}_{10}\text{Cr}_6\text{Al}_5$ alloy. In the simulation, at each temperature interval of 100 K from 1200 to 2500 K, a supercell containing 8100 atoms was equilibrated at the set temperature with the isothermal-isobaric (NPT) ensemble for 2×10^5 steps with a time step of 1 fs. Afterward, another 1×10^5 steps were performed to collect various quantities, such as system temperature and volume. The

cooling rate was 10^{12} K s $^{-1}$. The density of the liquid $\text{Ti}_{79}\text{Ni}_{10}\text{Cr}_6\text{Al}_5$ alloy can be calculated by the modified forms of Eq. (7),

$$\rho = \frac{m}{\langle V \rangle}, \quad (35)$$

where the angular bracket “ $\langle \rangle$ ” represents the ensemble average. The results calculated by different DNN potentials are presented in Fig. 15(a). Compared with the experimental results from our previous work,⁴⁷ the calculated values by DPT1-1 to DPT1-4 exhibited errors of 0.30%, 0.35%, 0.17%, and 0.13% at the T_L point, respectively. It can be observed that the computational accuracy of DNN potential is significantly superior to that of traditional empirical potential. Regardless of whether the “rcut_smth” is 0.5 or 5.8, whether the virial is included in the training or not, and whether it is supervised learning or active learning, these generated DNN potentials exhibited little difference in accuracy when predicting the density of the liquid $\text{Ti}_{79}\text{Ni}_{10}\text{Cr}_6\text{Al}_5$ alloy.

In the acquisition for the surface tension of the alloy, the surface tension σ was calculated by the following equation:⁴⁸

$$\sigma = \frac{V}{2A} \left\langle P_{zz} - \frac{1}{2}(P_{xx} + P_{yy}) \right\rangle, \quad (36)$$

where V is the volume, A is the area of the liquid-vapor interface, and P_{xx} , P_{yy} , and P_{zz} are the tangential components of the pressure tensor. The calculated results are illustrated in Fig. 15(b). It is evident that the DPT1-1 and DPT1-2 models have significant errors compared with the experimental results. The DPT1-1 exhibited 18.1% and 14.3% errors, and the DPT1-2 exhibited 31.1% and

26.0% errors at the T_L point when compared to the EML and ESL results, respectively. This indicates that the “rcut_smth” value and the inclusion of the virial term significantly impact the accuracy of the model’s predictions for the surface tension of liquid metals/alloys. Compared to DPT1-1 and DPT1-2, both DPT1-3 and DPT1-4 show a significant reduction in the error between their predicted results and experimental values. Additionally, DPT1-4 (1.9% with EML and 4.5% with ESL at the T_L point) demonstrated higher accuracy compared to DPT1-3 (2.5% with EML and 7.1% with ESL at the T_L point), even with a smaller training dataset. The test in surface tension manifested that strict “rcut_smth” values and incorporating the virial term during training can enhance the

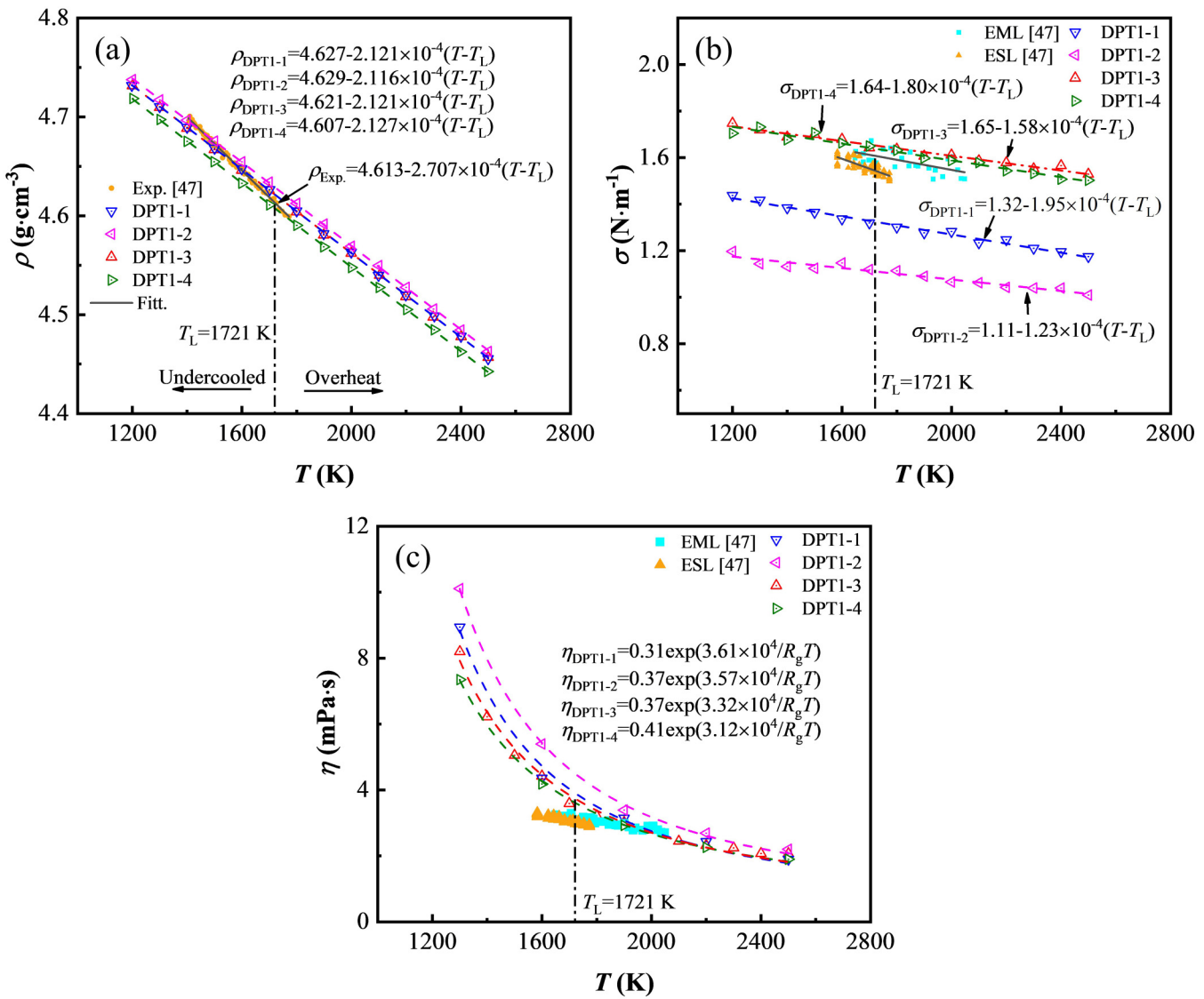


FIG. 15. Thermophysical properties of the liquid $\text{Ti}_{79}\text{Ni}_{10}\text{Cr}_{6}\text{Al}_5$ alloy: (a) density, (b) surface tension, and (c) viscosity.

25 November 2023 09:19:03

transferability of DNN potential, which enables DPT1-3 and DPT1-4 models to be applicable to systems involving interfaces. By adding configurations of the training dataset, such as the AIMD relaxation process of a system comprising two vacuum layers, one positioned above and one below, the prediction accuracy of DPT1-1 and DPT1-2 may also be improved.

The viscosity η can be calculated by the Green-Kubo equation⁴⁹

$$\eta = \frac{V}{Nk_B T} \int_0^\infty \langle P_i(t)P_i(0) \rangle dt, \quad (37)$$

where $P_i(t)$ represents the off-diagonal components of the atomic stress tensor at time t . Compared to the predictions using the Egry model,³¹ it appears that the viscosities calculated by DPT1-1 and DPT1-2 are slightly higher calculated values [Fig. 15(c)], while the results obtained by DPT1-3 and DPT1-4 are relatively closer to the reference values.

VI. CONCLUSIONS

In conclusion, we have provided a comprehensive guideline for acquiring thermophysical properties of liquid multicomponent alloys. This Tutorial offers an overview of both measurement technologies and DNN potential methodology at the beginning. Afterward, four DNN potentials were trained by different parameters and methods as an example to accurately predict the thermophysical properties of the liquid Ti₇₉Ni₁₀Cr₆Al₅ alloy. The results indicate that the “rcut_smth” value and the inclusion of virial term significantly influence the accuracy of DNN potentials, particularly in the case of surface tension prediction. Moreover, despite the use of a smaller training dataset, the DNN potential generated by the active learning method achieves a comparable level of prediction accuracy in contrast to the supervised learning approach. This means that, compared to solely relying on a large quantity of similar structures, the active learning process and the dataset diversity are more advantageous for the efficient and accurate construction of DNN potentials.

ACKNOWLEDGMENTS

Financial support from the National Natural Science Foundation of China (Grant Nos. 52225406, 52073232, and 52088101), the National Key Research and Development Program of China (Grant Nos. 2021YFB3700801 and 2021YFA0716301), and the Science Fund for Scientific and Technological Innovation Team of Shaanxi Province (Grant No. 2021TD-14), and the discussions from Mr. Q. Wang, Mr. J. F. Zhao, Mr. B. Zhai, and Mr. C. H. Zheng are acknowledged.

AUTHOR DECLARATIONS

Conflict of Interest

The authors have no conflicts to disclose.

Author Contributions

R. L. Xiao: Conceptualization (equal); Formal analysis (equal); Investigation (equal); Methodology (equal); Visualization (equal); Writing – original draft (lead). **K. L. Liu:** Formal analysis (equal); Methodology (equal); Validation (equal). **Y. Ruan:** Conceptualization (equal); Funding acquisition (equal); Investigation (equal); Supervision (equal); Writing – review & editing (equal). **L. Hu:** Methodology (equal); Validation (equal). **B. Wei:** Funding acquisition (equal); Resources (equal); Supervision (equal); Writing – review & editing (equal).

DATA AVAILABILITY

The data that support the findings of this study are available from the corresponding author upon reasonable request.

REFERENCES

- ¹V. V. Karasiev, J. Hinz, S. X. Hu, and S. B. Trickey, “On the liquid-liquid phase transition of dense hydrogen,” *Nature* **600**(7889), E12–E14 (2021).
- ²M. Lerbinger, A. Barbot, D. Vandembroucq, and S. Patinet, “Relevance of shear transformations in the relaxation of supercooled liquids,” *Phys. Rev. Lett.* **129**(19), 195501 (2022).
- ³R. Novakovic and J. Brillo, “Thermodynamics, thermophysical and structural properties of liquid Fe-Cr alloys,” *J. Mol. Liq.* **200**, 153–159 (2014).
- ⁴F. Xiao, K. Mukai, L. Fang, Y. Fu, and R. H. Yang, “Measurement and analyses of molten Ni-Co alloy density,” *Trans. Nonferrous Met. Soc. China* **16**(6), 1263–1267 (2006).
- ⁵H. M. Chen, Q. Wang, D. L. Geng, and H. P. Wang, “Specific heat, thermal diffusivity, and thermal conductivity of Ag-Si alloys within a wide temperature range of 293–823 K,” *J. Phys. Chem. Solids* **153**, 109997 (2021).
- ⁶Z. Moser, W. Gasior, and J. Pstrus, “Surface tension measurements of the Bi-Sn and Sn-Bi-Ag liquid alloys,” *J. Electron. Mater.* **30**(9), 1104–1111 (2001).
- ⁷V. M. B. Nunes, M. J. V. Lourenço, F. J. V. Santos, and C. A. Nieto de Castro, “Viscosity of industrially important Al-Zn alloys I-Quasi-eutectic alloys,” *Int. J. Thermophys.* **31**(11–12), 2348–2360 (2010).
- ⁸W. Li, S. Zhu, C. Wang, M. Chen, M. Shen, and F. Wang, “SiO₂-Al₂O₃-glass composite coating on Ti-6Al-4 V alloy: Oxidation and interfacial reaction behavior,” *Corros. Sci.* **74**, 367–378 (2013).
- ⁹M. Leitner, T. Leitner, A. Schmon, K. Aziz, and G. Pottlacher, “Thermophysical properties of liquid aluminum,” *Metall. Mater. Trans. A* **48**(6), 3036–3045 (2017).
- ¹⁰B. Reiplinger, Y. Plevachuk, and J. Brillo, “Surface tension of liquid Ti, V and their binary alloys measured by electromagnetic levitation,” *J. Mater. Sci.* **57**(47), 21828–21840 (2022).
- ¹¹H. P. Wang, J. Chang, and B. Wei, “Measurement and calculation of surface tension for undercooled liquid nickel and its alloy,” *J. Appl. Phys.* **106**(3), 033506 (2009).
- ¹²P.-F. Paradis, T. Ishikawa, G.-W. Lee, D. Holland-Moritz, J. Brillo, W.-K. Rhim, and J. T. Okada, “Materials properties measurements and particle beam interactions studies using electrostatic levitation,” *Mater. Sci. Eng. R Rep.* **76**, 1–53 (2014).
- ¹³T. Ishikawa, P.-F. Paradis, T. Itami, and S. Yoda, “Thermophysical properties of liquid refractory metals: Comparison between hard sphere model calculation and electrostatic levitation measurements,” *J. Chem. Phys.* **118**(17), 7912–7920 (2003).
- ¹⁴C. H. Zheng, P. F. Zou, L. Hu, H. P. Wang, and B. Wei, “Composition dependence of thermophysical properties for liquid Zr-V alloys determined at electrostatic levitation state,” *J. Appl. Phys.* **131**(16), 165104 (2022).

- ¹⁵S. Plimpton, "Fast parallel algorithms for short-range molecular dynamics," *J. Comput. Phys.* **117**(1), 1–19 (1995).
- ¹⁶G. Kresse and J. Furthmüller, "Efficient iterative schemes for *ab initio* total-energy calculations using a plane-wave basis set," *Phys. Rev. B* **54**(16), 11169–11186 (1996).
- ¹⁷H. Wang, L. F. Zhang, J. Q. Han, and E. Weinan, "DeePMD-kit: A deep learning package for many-body potential energy representation and molecular dynamics," *Comput. Phys. Commun.* **228**, 178–184 (2018).
- ¹⁸L. Lu, M. Dao, P. Kumar, U. Ramamurti, G. E. Karniadakis, and S. Suresh, "Extraction of mechanical properties of materials through deep learning from instrumented indentation," *Proc. Natl. Acad. Sci. U.S.A.* **117**(13), 7052–7062 (2020).
- ¹⁹E. Zhang, M. Dao, G. E. Karniadakis, and S. Suresh, "Analyses of internal structures and defects in materials using physics-informed neural networks," *Sci. Adv.* **8**(7), eabk0644 (2022).
- ²⁰P. Raccuglia, K. C. Elbert, P. D. Adler, C. Falk, M. B. Wenny, A. Mollo, M. Zeller, S. A. Friedler, J. Schrier, and A. J. Norquist, "Machine-learning-assisted materials discovery using failed experiments," *Nature* **533**(7601), 73–76 (2016).
- ²¹R. L. Xiao, K. L. Liu, Y. Ruan, and B. Wei, "Rapid acquisition of liquid thermophysical properties from pure metals to quaternary alloys by proposing a machine learning strategy," *Appl. Phys. Lett.* **123**(5), 052204 (2023).
- ²²Y. Z. Zhang, H. D. Wang, W. J. Chen, J. Z. Zeng, L. F. Zhang, H. Wang, and E. Weinan, "DP-GEN: A concurrent learning platform for the generation of reliable deep learning based potential energy models," *Comput. Phys. Commun.* **253**, 107206 (2020).
- ²³I. Egry, E. Ricci, R. Novakovic, and S. Ozawa, "Surface tension of liquid metals and alloys—recent developments," *Adv. Colloid Interface Sci.* **159**(2), 198–212 (2010).
- ²⁴B. S. Ashwin, T. Hagyard, I. C. B. Saunders, and T. E. Young, "Viscometers having damped torsional oscillation," *J. Sci. Instrum.* **37**(12), 480–485 (1960).
- ²⁵B. Reiplinger and J. Brillo, "Density and excess volume of the liquid Ti–V system measured in electromagnetic levitation," *J. Mater. Sci.* **57**(16), 7954–7964 (2022).
- ²⁶J. Brillo and I. Egry, "Density determination of liquid copper, nickel, and their alloys," *Int. J. Thermophys.* **24**(4), 1155–1170 (2003).
- ²⁷K. Zhou, H. P. Wang, J. Chang, and B. Wei, "Experimental study of surface tension, specific heat and thermal diffusivity of liquid and solid titanium," *Chem. Phys. Lett.* **639**, 105–108 (2015).
- ²⁸M. Watanabe, M. Adachi, and H. Fukuyama, "Heat capacities and thermal conductivities of palladium and titanium melts and correlation between thermal diffusivity and density of states for transition metals in a liquid state," *J. Mol. Liq.* **324**, 115138 (2021).
- ²⁹J. Brillo, G. Lohofer, F. Schmidt-Hohagen, S. Schneider, and I. Egry, "Thermophysical property measurements of liquid metals by electromagnetic levitation," *Int. J. Mater. Prod. Technol.* **26**(3–4), 247–273 (2006).
- ³⁰D. L. Cummings and D. A. Blackburn, "Oscillations of magnetically levitated aspherical droplets," *J. Fluid Mech.* **224**, 395–416 (1991).
- ³¹I. Egry, "On the relation between surface tension and viscosity for liquid metals," *Scr. Metall. Mater.* **28**(10), 1273–1276 (1993).
- ³²L. Wang, L. Hu, S. J. Yang, and B. Wei, "Liquid state property and intermetallic compound growth of Zr₂Ni alloy investigated under electrostatic levitation condition," *Chem. Phys. Lett.* **711**, 227–230 (2018).
- ³³A. J. Rulison and W.-K. Rhim, "A noncontact measurement technique for the specific heat and total hemispherical emissivity of undercooled refractory materials," *Rev. Sci. Instrum.* **65**(3), 695–700 (1994).
- ³⁴J. Q. Feng and K. V. Beard, "Small-amplitude oscillations of electrostatically levitated drops," *Proc. R. Soc. London, Ser. A* **430**(1878), 133–150 (1990).
- ³⁵M. Mohr, R. Wunderlich, R. Novakovic, E. Ricci, and H.-J. Fecht, "Precise measurements of thermophysical properties of liquid Ti–6Al–4 V (Ti64) alloy on board the international space station," *Adv. Eng. Mater.* **22**(7), 2000169 (2020).
- ³⁶J. Nawer, T. Ishikawa, H. Oda, H. Saruwatari, C. Koyama, X. Xiao, S. Schneider, M. Kolbe, and D. M. Matson, "Uncertainty analysis and performance evaluation of thermophysical property measurement of liquid Au in microgravity," *npj Microgravity* **9**(1), 38 (2023).
- ³⁷D. C. Van Hoesen, A. K. Gangopadhyay, G. Löhöfer, M. E. Sellers, C. E. Pueblo, S. Koch, P. K. Galenko, and K. F. Kelton, "Resistivity saturation in metallic liquids above a dynamical crossover temperature observed in measurements aboard the International Space Station," *Phys. Rev. Lett.* **123**(22), 226601 (2019).
- ³⁸T. Ishikawa, P.-F. Paradis, and C. Koyama, "Thermophysical property measurements of refractory oxide melts With an electrostatic levitation furnace in the international space station," *Front. Mater.* **9**, 954126 (2022).
- ³⁹M. Mohr, R. K. Wunderlich, D. C. Hofmann, and H. J. Fecht, "Thermophysical properties of liquid Zr_{52.5}Cu_{17.9}Ni_{14.6}Al₁₀Ti₅-prospects for bulk metallic glass manufacturing in space," *npj Microgravity* **5**, 24 (2019).
- ⁴⁰C. Koyama, T. Ishikawa, H. Oda, H. Saruwatari, S. Ueno, M. Oshio, Y. Watanabe, and Y. Nakata, "Densities of liquid lanthanoid sesquioxides measured with the electrostatic levitation furnace in the ISS," *J. Am. Ceram. Soc.* **104**(7), 2913–2918 (2021).
- ⁴¹F. Rosenblatt, "The perceptron: A probabilistic model for information storage and organization in the brain," *Psychol. Rev.* **65**(6), 386–408 (1958).
- ⁴²J. Z. Zeng, D. Zhang, D. H. Lu *et al.*, "DeePMD-kit v2: A software package for deep potential models," *J. Chem. Phys.* **159**(5), 054801 (2023).
- ⁴³See <https://github.com/deepmodeling/dpdata> for dpdata software.
- ⁴⁴See https://github.com/deepmodeling/deepmd-kit/blob/master/examples/water/se_e2_a/input.json for JSON example file to set training procedure of DeePMD-kit software.
- ⁴⁵See <https://github.com/deepmodeling/dpgen/blob/master/examples/machine/> for information about JSON example file to specify the machine environment for DP-GEN software.
- ⁴⁶See <https://github.com/deepmodeling/dpgen/blob/master/examples/run> for information about for JSON example file to set the training procedure for DP-GEN software.
- ⁴⁷R. L. Xiao, Q. Wang, J. Y. Qin, J. F. Zhao, Y. Ruan, H. P. Wang, H. Li, and B. Wei, "A deep learning approach to predict thermophysical properties of metastable liquid Ti–Ni–Cr–Al alloy," *J. Appl. Phys.* **133**(8), 085102 (2023).
- ⁴⁸M. J. P. Nijmeijer, A. F. Bakker, C. Bruin, and J. H. Sikkenk, "A molecular dynamics simulation of the Lennard-Jones liquid-vapor interface," *J. Chem. Phys.* **89**(6), 3789–3792 (1988).
- ⁴⁹Y. Zhang, A. Otani, and E. J. Maginn, "Reliable viscosity calculation from equilibrium molecular dynamics simulations: A time decomposition method," *J. Chem. Theory Comput.* **11**(8), 3537–3546 (2015).